Pergamon

Journal of Structural Geology, Vol. 16, No. 7, pp. 1007 to 1021, 1994

0191-8141/94 $07.00+0.00

Rheological controls on the shapes of single-layer folds

PETER J. HUDLESTON and LABAO LAN

Department of Geology and Geophysics, University of Minnesota, Minneapolis, MN 55455, U.S.A.

(*Received* 4 *February* 1992; *accepted in revised form* 19 *August* 1993)

Abstract—Information about rheology can potentially be gained from analyzing the shapes of folds in isolated buckled layers. We employ two-dimensional finite element models of incompressible flow in power-law viscous fluids to investigate this. We first show that the shape of the initial perturbation has relatively little effect on the final shape of the folds when the buckling instability is high. We find that the most significant factor affecting the shapes of single-layer folds is the stress exponent, n_L, in the flow law of the layer. The hinges of outer arcs become sharper as n_L increases and the limbs become relatively longer and straighter. These differences can be expressed quantitatively by defining a curvature index, *ki*, which has a value of 0 for a fold formed by circular arcs and 1 for a chevron fold. Results show a dependence of *ki* on n_L that is well-defined for $L/h > 10$, with *ki* increasing with n_L. Data for experimentally-produced folds are consistent with the numerical results.

Limb dip, *ki* and *L/h* can all be readily measured on natural folds and provide a basis for comparing the shapes of natural and computer-simulated folds. The data for small folds in siltstone layers in shales in the central Appalachians are consistent with highly non-linear flow of the stiff siltstone layers during buckling.

INTRODUCTION

IN THE last 30 years or so, beginning with the work of Biot (1957, 1961) and Ramberg (1961, 1963a), theoretical, physical and numerical models have led to a greatly increased understanding of the mechanisms of folding in layered materials. It is difficult, however, to assess the relevance of these models to folding in nature because we do not know what the rheological properties of the rocks were at the time of folding. We can gain some understanding of the processes responsible for folding in nature by seeing how closely natural folds compare with folds produced in experimental and numerical models, in terms of their shape, wavelength/thickness characteristics and strain distribution (e.g. Ramsay 1967, chap. 7, Hudleston 1973a,b, Ramsay & Huber 1987, Cruikshank & Johnson 1993, Hudleston & Lan 1993), and by seeing how well natural folds match the predictions of folding theory (e.g. Sherwin & Chapple 1968, Fletcher 1974, Fletcher & Sherwin 1978, Hudleston & Tabor 1988, Johnson & Pfaff 1989). From this work, we believe that many natural folds are initiated by *buckling*, a mechanical instability that may develop when layered materials (of elastic, viscous or more complex type of constitutive relationship) are subjected to layer-parallel compression (e.g. Biot 1961, Ramberg 1963a). Buckle folds can develop in isolated stiff layers in a less stiff matrix or in multilayered packages, in which individual layers vary in composition (and thus in stiffness) and thickness. They may also develop in homogeneous but anisotropic materials (Cobbold *et al.* 1971, Ridley & Casey 1989).

Single-layer folds are much less variable in shape than multilayer folds, and we restrict our investigation in this paper to folds developed by the buckling of a single isolated viscous layer in a less viscous matrix. The purpose of the paper is to explore how rheological properties affect the shape of such folds and to seek criteria based on shape that may be able to provide information about rheological properties of rocks deformed under slow natural conditions.

It is pertinent to review some features of the theoretical treatment of the single-layer configuration. For very slow natural deformations one is justified in ignoring inertial forces, and it is usual also to ignore gravitational body forces for small structures (Ramberg 1970, but see Wollkind & Alexander 1982). Theory predicts that, for a system consisting of an extensive isolated stiff viscous layer in a less viscous matrix subject to layer-parallel pure shear, all harmonic components that are present in the initial irregularities of the layer interfaces will become amplified, with a maximum rate of growth occurring for the 'dominant wavelength' (Biot 1961, Ramberg 1963b, Fletcher 1974, Smith 1975). For Newtonian materials, the ratio of dominant wavelength to thickness is a function only of the ratio of viscosity of the stiff layer to the viscosity of the matrix. Wavelength and thickness both change with time as a consequence of the uniform base flow on which the bucking instability is superimposed (Sherwin & Chapple 1968, Fletcher 1974), and the harmonic component that experiences the greatest amplification is also a function of time or, more conveniently, of the uniform shortening upon which the buckling instability is superimposed (Sherwin & Chapple 1968, Fletcher 1974, Johnson & Pfaff 1989). The wavelength that shows the greatest amplification is called the 'preferred wavelength' by Fletcher (1974), and this wavelength varies with shortening. A simple relationship between dominant wavelength and preferred wavelength is given by Johnson & Pfaff (1989, equation 27a).

For non-linear viscous materials, fold amplification, and hence also both the dominant wavelength/thickness

and the preferred wavelength/thickness, is found to depend strongly on the stress exponent in the flow law of both layer and matrix when the constitutive relationships are of power-law type (Fletcher 1974), or the effective stress exponents in flow laws of more general non-linear type (Smith 1977).

Experimental work confirms the tendency of buckling in single viscous layers to develop periodic folds (Biot *et al.* 1961, Hudleston 1973b, Neurath & Smith 1982), and analysis of fold growth from an initial local bell-shaped perturbation indicates close agreement to the theoretical predictions for the independent amplification of the harmonic components representing the perturbation (Abbassi & Mancktelow 1992, Mancktelow & Abbassi 1992).

Wavelength/thickness frequency spectra for natural single-layer folds are similar in appearance to theoretical amplification spectra (Sherwin & Chapple 1968), and studies of wavelength/thickness spectra in natural folds, particularly when done in conjunction with estimates of layer-parallel shortening, have been carried out to arrive at estimates of viscosity contrast and inferences about the degree of non-linearity of the flow law (e.g. Fletcher 1974, Hudleston & Holst 1984, Holst 1987, Hudleston & Tabor 1988). One of the questions raised by such studies, however, is just how closely the frequency distribution of arc-length/thickness measured in mature fold trains is related to the theoretical amplification spectrum of wavelength/thickness (Fletcher & Sherwin 1978). There is in particular uncertainty about the form of the spectrum of the initial irregularities in the layers which, with the amplification spectrum, determines the final amplitude spectrum.

In this paper, we systematically investigate how the shapes of single-layer folds in power-law materials depend on the stress exponent of the layer and on the ratio of viscosities of layer and matrix. A prime objective is to identify characteristics of folds, other than wavelength/thickness ratio, that depend on the rheological properties of the layers, with the idea that these characteristics may be used to make inferences about rheological properties of rocks during natural folding. The current work is part of a broader study of the development of folds in non-linear viscous media (see Lan & Hudleston 1991, Hudleston & Lan 1993). Partial results of what is presented here have been given in Hudleston & Lan (1993).

METHODS OF CHARACTERIZING FOLD SHAPE

Various methods of describing or characterizing the geometrical characteristics of folds have been proposed over the years, starting with Van Hise (1896a, b), who named and described similar folds and parallel folds. Others to address the topic include Mertie (1959), Fleuty (1964), Ramsay (1967), Wilson (1967), Stabler (1968), Hudleston (1973a), Ramsay & Huber (1987), Twiss (1988), Johnson & Pfaff (1989) and Bastida (1993). Ramsay (1967, chap. 7) provided a good review of early work on folds and introduced several methods for representing fold shape. He made the distinction between 'layer' shape and 'surface' shape, and it is the shapes of the two surfaces bounding a single folded layer that we emphasize in this paper. Several workers have used Fourier series to analyze and represent fold shapes. Stabler (1968) and Hudleston (1973a) both used the sine terms of a Fourier series to characterize single-surface fold shapes, and Fletcher (1979) and Johnson & Pfaff (1989) have used the cosine terms to analyze fold shape (layer and surface) and its changes during fold growth at low to moderate amplitudes.

Except for similar folds, the outer and inner arcs of folds in any given layer will differ in shape. However, a complete train—upper and lower surfaces—of periodic symmetric folds can be generated by taking a section of (upper or lower) surface between two adjacent hinges and performing on this appropriate symmetry operations. The basic segment we choose for sine series harmonic analysis is the 'quarter wavelength' between hinge point and inflexion point, with the origin of the coordinates at the inflexion point. For this analysis, the folds must be cylindrical and examined in a section perpendicular to the hinge. Many natural folds approach this condition, although non-cylindrical folds are also common (e.g. Wilson 1967). Utilizing a quarter wavelength segment of a fold, expanded to become periodic, all coefficients except odd terms in the sine series are zero. Thus the harmonic series, $F(x)$, representing the fold becomes (Hudleston 1973a):

$$F(x) = b_1 \sin\frac{2\pi x}{L} + b_3 \sin\frac{2\pi 3x}{L} + b_5 \sin\frac{2\pi 5x}{L} \ldots + b_n \sin\frac{2\pi nx}{L}, \quad (1)$$

where L is the wavelength and b_n are the coefficients whose values define fold shape in an x–y Cartesian coordinate system. With this approach, the inner and outer arcs of a single fold are treated separately and will in general have different values of the coefficients. This may be compared with the approach taken by Fletcher (1979), Johnson & Pfaff (1989) and Cruikshank & Johnson (1993), who employed both even and odd terms of a cosine series

$$F(x) = a_0 + a_1 \cos\frac{2\pi x}{L} + a_2 \cos\frac{2\pi 2x}{L} + a_3 \cos\frac{2\pi 3x}{L} \ldots + a_n \cos\frac{2\pi nx}{L}, \quad (2)$$

with origin on the axial surface trace and with all sine terms zero, which allowed them to represent a complete upper or lower surface of periodic folds with anticlinal and synclinal portions of different shape, as occurs in parallel folds. At low amplitudes the parallel form is produced by the first harmonic, with a_2 being of opposite sign for the upper and lower surfaces of the layer (Fletcher 1979). For studying growth rates of folds, a cosine series representation is preferable: for character-

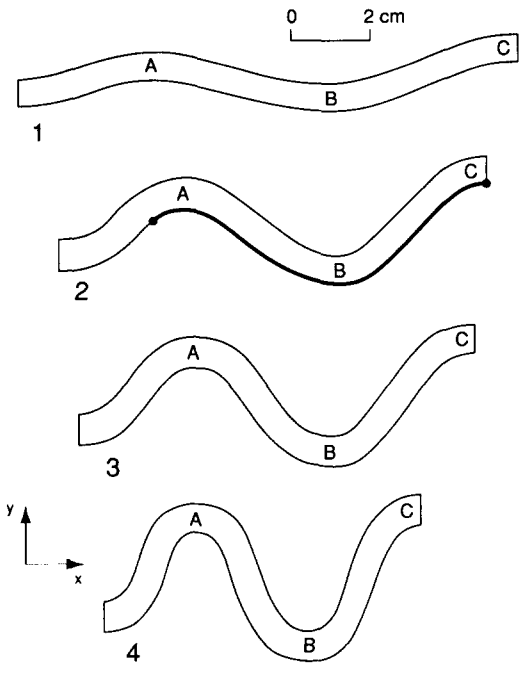

Fig. 1. Buckle folds at four stages of development produced in experiments with Newtonian stiff layers and matrix, with effective viscosity ratio $\mu_L/\mu_M = 50$ (see Hudleston 1973b for details of experiments). Curvature of the section of layer surface shown with a heavy line is plotted against x in Fig. 3.

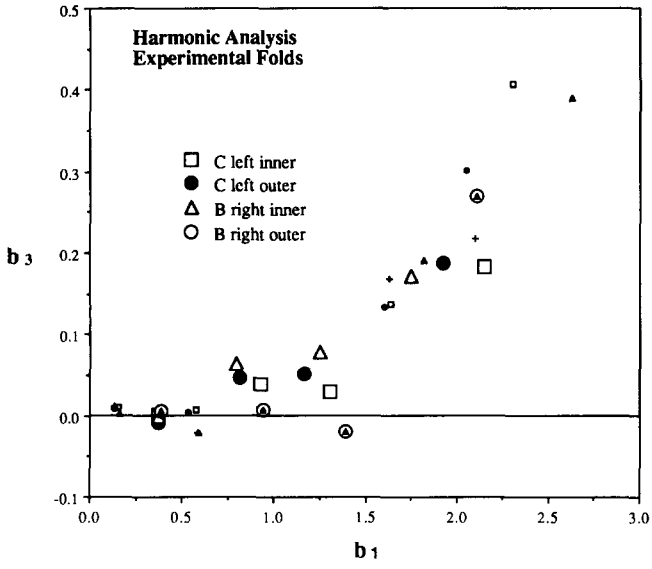

Fig. 2. Plot of harmonic coefficients b_3 against b_1 for the folds B and C shown in Fig. 1 and the same folds at other stages of fold development not illustrated. Data for the folds not shown in Fig. 1 are plotted with small symbols. Note that the folds do not depart significantly from a sinusoidal shape ($b_3 = 0$) until after stage 3.

izing shape with as few parameters as possible, use of the first two terms in a sine series is advantageous. Both representations are referred to below.

The ratio b_3/b_1, or slope on a graph of b_3 against b_1, is a sensitive indicator of shape, varying from negative values for straight-limbed folds, through zero for sinusoidal shapes, to positive for folds with rounded hinges and short limbs (Figs. 1 and 2). A wide range of single-surface fold shapes, for which the harmonic coefficients in the higher terms in the series decrease in systematic manner (with continuous variation in shape through the range) can be uniquely represented by the value of b_1 and the ratio b_3/b_1 (Hudleston 1973a, fig. 9). Other shapes of course are possible, and Twiss (1988) has shown that the range of fold shapes represented by b_1 and b_3/b_1 can be placed in a more general descriptive scheme. It should be noted that a_3 modifies shape in the same way as does b_3, and a plot of a_3 against a_1 is analogous to one of b_3 against b_1, noting the difference in origin between the two harmonic series.

There are other methods that for some purposes may be more suitable than harmonic analysis in quantifying single-surface shape variations. Ramsay (1967, p. 350) developed parameters of fold shape P_1 and P_2 based on curvature. He proposed a definition of the hinge zone of a fold surface as that part with curvature in excess of the reference curvature of a circle (i.e. the reciprocal of the radius) that has as its diameter the line joining the inflexion points either side of the hinge. The limbs of the fold are those parts with curvature less than the reference curvature. P_1 is then defined as the ratio of the length of the projection of the limbs on the line joining the inflexion points to the length of the projection of the hinge zone on the same line. P_2 is the ratio of the maximum curvature of the fold surface to the reference curvature. One disadvantage of P_1 and P_2 is that the values of both tend to infinity as the hinge zone approaches a point, which is the situation for a perfect chevron shape. We adopt a somewhat different approach here. Curvature, $k(x)$, is defined by (e.g. Leithold 1981, p. 878):

$$k(x) = \frac{d^2y/dx^2}{[1 + (dy/dx)^2]^{3/2}}. \quad (3)$$

We calculate curvature by fitting low-degree polynomials to the x–y co-ordinates used to represent shapes (of natural, numerically-produced or experimentally-produced folds) and evaluate equation (3) for a best-fit polynomial. The object is to find the curvature of a smoothly varying function that represents the fold profile closely. This is best done in practice by taking 10–20 points per half 'wavelength' and piecewise fitting a second degree polynomial to three or five points to calculate curvature at the central point. This has been done in Fig. 3 for part of the experimental fold train indicated by a heavy line in stage 2 of Fig. 1. Because curvature involves the second derivative of the function representing fold shape, without the smoothing involved in an approach such as this, the function $k(x)$ for natural folds contains a lot of noise. Other techniques, including cubic splines (e.g. Kincaid & Cheney 1991, pp. 317–322), were tried, but deemed less suitable. The use of curvature, as here, in an analysis of fold shape in two dimensions should be contrasted with its use in describing three-dimensional fold surface shape (Lisle 1992).

Calculated curvature for the experimental folds in Fig. 1 can be compared with the plots of curvature plotted against distance from hinge to hinge for several ideal fold shapes shown in Figs. 4(b)–(d). One extreme

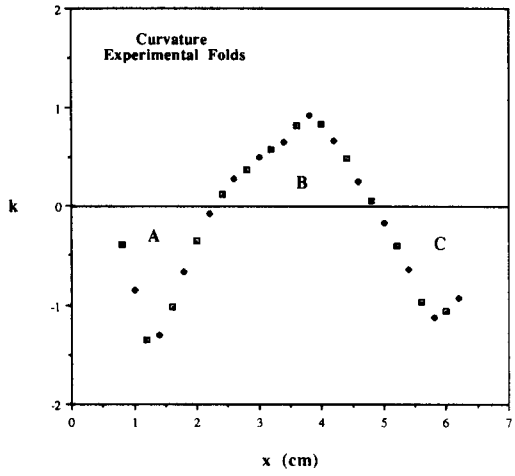

Fig. 3. Plot of curvature against x for the surface of the folds shown in Fig. 1 (stage 2) by a heavy line. The different symbols are for two separate sets of co-ordinate points used to represent the fold.

ideal shape is a fold formed by circular arcs with a discontinuity and change in sign of curvature at each inflexion point. A second is a pure chevron shape with limbs of zero curvature and infinite curvature at the hinge. These might be considered to correspond to folds that are all hinge and all limb, respectively. Comparison of Figs. 3 and 4 shows that the selected experimental fold is much closer in shape to a sinusoid than to either of the extreme shapes. The differences in pattern of curvature variation in these folds can be expressed using a curvature index, *ki*, which is defined here as the ratio of the distance between the inflexion point (where curvature is zero) and the point at which curvature attains, arbitrarily, 0.75 of its maximum value to the distance between the inflexion point and the hinge (where curvature is maximum). Distances are measured from the inflexion point to the projections of the points at which $k(x) = 0.75\ k_{max}$ and $k(x) = k_{max}$ (hinge) on an axis (x-co-ordinate) through the inflexion point and perpendicular to the axial plane (see Fig. 4a). This index has a value of 1 for a chevron fold, 0 for a fold formed by circular arcs, and 0.77 for the function, $y = \sin x$ (for sinusoidal functions of general form $y = a \sin x$, its values ranges between 0.54 and 1.0, corresponding to values of amplitude, a, of from near zero to infinity). It reflects the degree of flatness or roundness of the fold limbs and it cannot be uniquely expressed in terms of the coefficients of a Fourier series.

We also examine thickness variations in buckled layers in this paper, and the method we employ here for characterizing changes in folded layer thickness is to plot normalized orthogonal thickness, t'_α, against limb 'dip', α (Ramsay 1967, p. 360).

NUMERICAL MODELING

To investigate how fold shape depends on rheological parameters, we use a finite element code adapted from that developed by Hanson (1985, 1990) for simulating flow of glaciers. It treats the case of plane incompressible quasi-static flow in a power-law material. The basic application of this code to the study of the growth of single-layer buckle folds is described elsewhere (Lan & Hudleston 1991), and comparison of the results with theoretical predictions and with the results of earlier finite element models is given in that paper. Grids of 200–400 quadrilateral elements are used to represent a folded layer in its matrix, making use of symmetry in the construction of the grid. Tens to 100 iterations are required for convergence to a steady-state velocity solution for each increment of displacement (for non-linear rheology).

In what follows, the subscripts L and M refer to layer and matrix, respectively, and the subscript o refers to the initial stage. Wavelength and thickness are represented by L and h, respectively. They change in value as a result of deformation. The percentage shortening in the direction parallel to the layer is indicated by S. It is the shortening of the homogeneous strain that would result if only one material were present.

Three values (1, 3 and 10) of power-law exponent, n_L, of the stiff layer were selected, providing a range from Newtonian behavior to strongly non-linear, and covering the range of values commonly found in experimental work involving ductile deformation of rock (e.g. Kirby & Kronenberg 1987). Viscosity, μ, depends on stress level in non-linear materials, and will vary with position in both layer and matrix during folding. A viscosity ratio ($m = \mu_L/\mu_M$) of layer to matrix, however, can be defined for the basic flow (on which the perturbation flow associated with folding is superimposed), and values of m of 10, 215, 630, for $n_L = 1, 3, 10$, respectively, were taken for the first series of models. These three values of m for $n_L = 1, 3, 10$ correspond to a constant value of 10 for the quantity $D_M^{1/nM}/D_L^{1/nL}$, where D is the coefficient in the flow law, $\dot{e} = D\sigma^n$ (in which $\dot{e}$ and σ are the second invariants of the strain rate and stress tensors, respectively) and viscosity, $\mu = D^{-1/n}\dot{e}^{(1/n-1)}$. Models were run with constant strain rate for the base flow. A second series of models for values of m 10 times those of the first series ($m = 100, 2100, 6300$), and a third series for $\mu_L/\mu_M = 100$ for all three values of n_L were also run. Initial wavelength/thickness (L_o/h_o) was taken as an independent variable in these models, and values of $L_o/h_o = 6, 12, 20, 30$ were chosen to straddle the predicted dominant wavelength/thickness, L_d/h, and to cover typical values seen in nature. The parameters used and the theoretical dominant wavelength/thickness and preferred wavelength/thickness, L_p/h, at an amplification (amplitude/initial amplitude) of 40 for the various models are shown in Table 1. Individual runs involved shortening of up to 60% (or 75% for $n_L = 1$). For the basic experiments, the initial shape of the perturbation in both surfaces of the layer was identical and sinusoidal, with amplitude, A_o, of 0.083 L_o (based on $A_o = 0.1\ h_o$ for $L_o/h_o = 12$). Fletcher (1974) has shown theoretically that the power-law exponent, n_M, of the matrix has a small effect on the buckling instability, when the rheological parameters are appropriately expressed. In fact, the dynamic growth rate is increased at constant m as

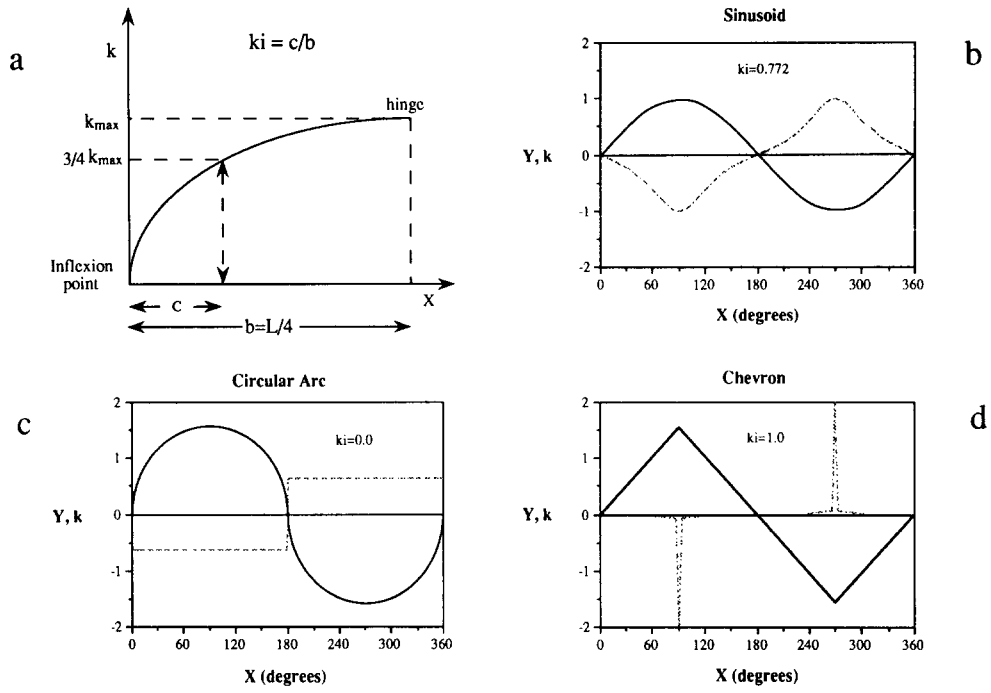

Fig. 4. Definition of curvature index, *ki* (a), and illustration of curvature and curvature index for three ideal fold shapes, (b) sinusoid, (c) circular arc and (d) chevron.

Table 1. Rheological parameters and geometrical data. The left three columns give the combinations of rheological parameters used in the numerical models. The fourth column is the theoretical dominant wavelength/thickness (using Fletcher's 1974 first-order theory). Columns 5 and 6 are values of the preferred wavelength/thickness, L_p/h, at an amplification of 40, and the shortening, S, at which this is attained. The last three columns are the *ratio* of amplification of folds for which $L_o/h_o = 6$, 12 and 20, respectively, to the maximum amplification (for the fold of the preferred wavelength/thickness)

n_L	n_M	m	L_d/h	L_p/h	S%	$\frac{A_{max}}{A_{L_o/h_o}=6}$	$\frac{A_{max}}{A_{L_o/h_o}=12}$	$\frac{A_{max}}{A_{L_o/h_o}=20}$
1	1	10	8.5	4.0	58.0	0.18	0.61	0.98
3	1	215	15.0	14.1	5.9	0.10	0.75	0.84
10	1	630	14.3	14.0	1.9	0.12	0.84	0.69
1	1	100	16.8	14.5	13.6	0.08	0.49	0.99
3	1	100	11.8	10.6	9.8	0.18	0.96	0.60
10	1	100	8.3	7.7	7.2	0.56	0.78	0.28

either n_L or n_M is increased, with the dominant wavelength/thickness decreasing as n_L is increased and increasing as n_M is increased (see Smith 1977, figs. 6 and 8). The matrix material was made linear viscous, $n_M = 1$, in all but a few cases in our models.

An example of the results of the numerical modeling is shown in Fig. 5, in which the progressive development of fold shape for Newtonian layer and matrix is displayed.

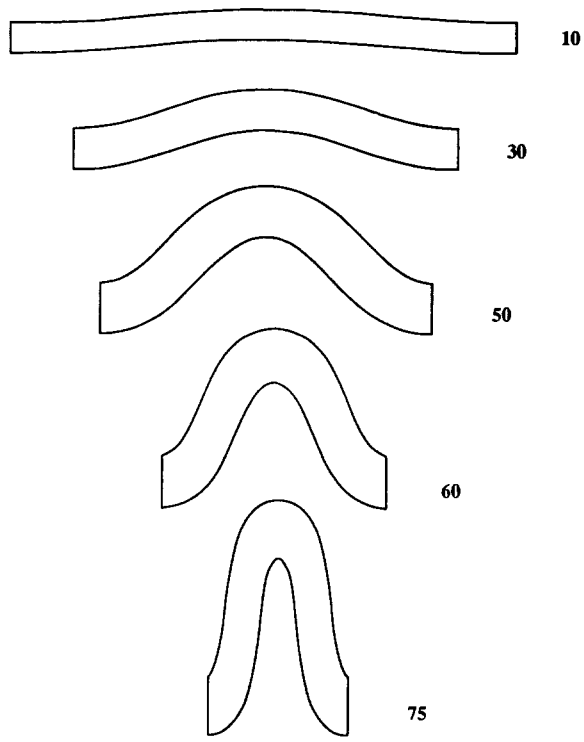

Fig. 5. Results of numerical modeling of a buckle fold developed in pure shear in a stiff layer embedded in a matrix, with $n_L = 1$, $\mu_L/\mu_M = m = 10$, $L_o/h_o = 20$, and $A_o = 0.167h_o$ at values of shortening, $S = 10$, 30, 50, 60 and 75%.

Effect of initial shape

If fold shape is to be used to provide information on rheological conditions, it is imperative to evaluate the effect of the shape of the initial perturbation on final fold shape. We have done this by running numerical models with four initial perturbations of different shape, all of low amplitude, and all periodic. These are sinusoid, chevron, semi-ellipse, and bell. These can be considered to represent higher-order perturbations on a 'primary' wavelength that is within the band of wavelengths most strongly amplified early in the folding process. The 'primary' wavelength is not necessarily the dominant wavelength or the wavelength that will become the preferred wavelength at some specified value of shortening, but the further it is from the preferred wavelength the less the probability of such a wavelength being present in a natural fold train (see Fletcher & Sherwin

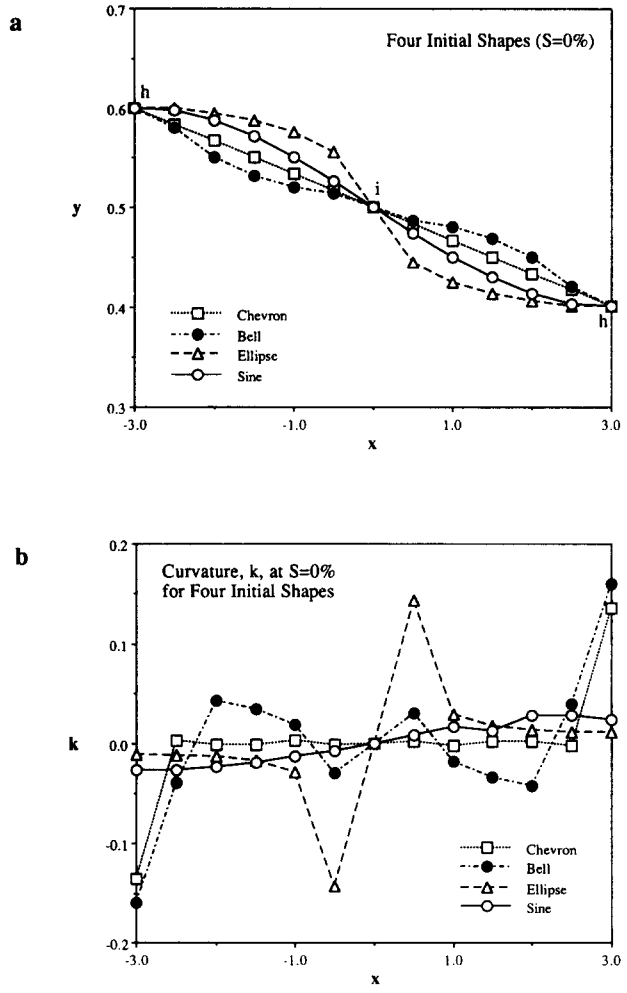

Fig. 6. (a) Four different initial perturbations of the upper surface of the stiff layer (both upper and lower surfaces of the layer have the same initial shape) from anticlinal to synclinal hinges, with a vertical exaggeration of about × 10 to emphasize the differences. In all cases $L_o/h_o = 12$ and $A_o = 0.1h_o$. The functions are defined as follows ($-3 \leq x \leq 3$): sinusoid—$y = -0.1\sin(\pi/6)x$; chevron—$y = -0.033x$; semi-ellipse—$y = \pm 0.033[3^2-(x\pm 3)^2]^{1/2}$; bell—$y = \pm 0.1[1+(x\pm 3)^2]^{-1}$. The inflexion point is indicated by i, and the hinges by h. The origin of the co-ordinate system (0,0) here and in Fig. 7 is in the center of the layer at the inflexion point. The scale is arbitrary. (b) Curvature variations for the initial shapes shown in (a).

(1978) and, for example the frequency distributions of wavelength/thickness in Sherwin & Chapple (1968) and Hudleston & Holst (1984)). In taking this approach we are separating the process of selective growth of a 'primary' wavelength from the subsequent modification of the selected wavelength by higher order harmonics as the fold grows (see Fletcher 1979, 1982, Johnson & Pfaff 1989). It is the nature of this subsequent modification that we study here.

Initial single-surface shapes and corresponding curvature variations are shown in Fig. 6 and the mathematical definitions are given in the caption to that figure. Initial 'primary' wavelength/thickness ratio ($L_o/h_o = 12$) was the same for all models, and viscosity ratio was taken as $m = 10, 215, 630$, for $n_L = 1, 3, 10$, respectively. Results are shown in Figs. 7–10 for $n_L = 1$ and 10. Both chevron and bell shapes have sharp hinges and rapid drops in curvature towards the inflexion points. The bell shape has subsidiary hinges either side of the inflexion point, a situation that thus represents weak parasitic folds on the limb of a larger fold. The reader should note that in this usage the bell curve is truncated and made periodic, unlike the bell curve used by Biot *et al.* (1961) and Abbassi & Mancktelow (1992) to simulate a single local perturbation. The semi-ellipse, with long axis parallel to x, is a double-hinged fold with the hinges lying close to the inflexion points. The crest (or trough) of the fold, which is the 'hinge' for the purpose of analysis, is in fact the point of minimum curvature between two anticlinal (or synclinal) hinges. These initial shapes thus provide a wide range of starting configurations. Note, however, that all are symmetric about the principal axial planes. The effect of asymmetry about the axial plane is not investigated here, but will be addressed briefly in the discussion section. It has been investigated experimentally (Abbassi & Mancktelow 1990). Likewise, we do not consider here the growth of the harmonic components in a complete spectrum of initial irregularities, as done by Fletcher & Sherwin (1978).

Mature fold shapes after 60% shortening for $n_L = 1$ and 10 are shown in Fig. 7. Only the upper surface of the competent layer, except for the 'sine wave' models, is shown, because the lower surface is identical in shape to the upper surface and can be obtained from it by a rotation of 180° about the center of the plot. It is apparent that there is very little difference in shape among the four folds for $n_L = 10$ and $m = 630$. There are much greater differences among the four folds for $n_L = 1$ and $m = 10$, although the differences in outer arc shape are not large: the differences in the inner arc are more pronounced. The greater buckling instability for $n_L = 10$ and $m = 630$ is reflected in the higher fold amplitudes (compare Figs. 7a & b).

Progressive changes in shape with overall shortening, as recorded by harmonic analysis and curvature variations, are shown in Figs. 8–10. Note that the differences among the four models are rapidly diminished as shortening progresses for $n_L = 10$ and $m = 630$, whereas the differences are diminished much more slowly for $n_L = 1$ and $m = 10$. Take the example of the 'ellipse' starting shape. For $n_L = 10$, by 10% shortening the curvature maxima and minima are at the 'proper' hinge positions, that is at the crest and trough of the folds, and the original hinges of the double-hinged fold adjacent to the inflexion point are of secondary importance (Fig. 9b). For $n_L = 1$, the folds are still double-hinged at 10% shortening (Fig. 9a), and indeed also at 40% shortening (not shown). By 60% shortening, however, the hinges are in the proper locations (Fig. 9c) at the fold crest and trough.

Plots of b_3/b_1 (Fig. 8) and ki (Fig. 10) against shortening show the same general features—a rapid convergence to a preferred shape (which itself changes with shortening) for $n_L = 10$ and a slow convergence to a preferred shape for $n_L = 1$. For $n_L = 10$, b_3 initially changes much less than b_1, and b_3/b_1 becomes small, indicating the initial dominance of the 'primary' wavelength. In fact b_3 becomes slightly negative in all cases, indicating fold shapes with slightly sharper hinges and

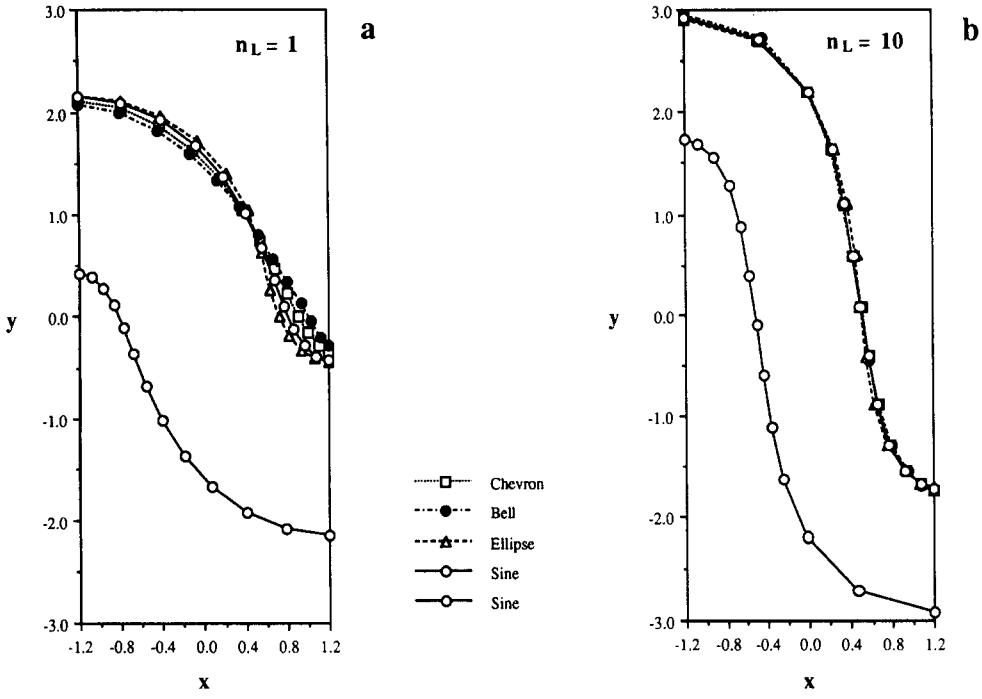

Fig. 7. Mature shapes of the upper surfaces of folds from anticlinal (left) to synclinal (right) hinges, developed from the initial perturbations shown in Fig. 6(a) after 60% shortening for (a) $n_L = 1$, $m = 10$ and (b) $n_L = 10$, $m = 630$. The lower surface of the fold in the stiff layer is shown in (a) and (b) for the initial sine shape only. In all cases, the lower surface of the fold can be generated from the upper by a 180° rotation about the origin. The difference between (a) and (b) in layer thickness reflects the difference in early layer shortening and thickening, which is greater for the weak buckling instability represented by (a). Figure 5 shows how early layer shortening and thickening occurs.

straighter limbs than a sine function. This effect is most pronounced at about 10% shortening. Subsequently b_3 increases, and by $S = 20\%$ (limb dips of about 40–50°), all the folds are close to sinusoidal in shape (b_3/b_1 increases). As is typical for buckle folds, the b_3 vs b_1 plots are strongly concave upwards.

For comparison with Fig. 8, if $m = 1$ and $n_L = 1$, the layer and the matrix would become identical and the layer boundaries passive markers. Thus, the initial perturbations would be amplified passively; on a harmonic plot (such as Fig. 8) their shapes would lie on straight lines of constant 'shape' passing through the origin (see Hudleston 1973a).

We conclude from this analysis that when buckling instabilities are high ($n_L = 3, m = 215$—not shown—and $n_L = 10, m = 630$) the initial form of the perturbation in the layer has a relatively small effect on the shape of the mature folds once a 'primary' wavelength has been selected. This encourages us to examine further the shapes of mature folds to see how strongly they depend on the values of n_L and m.

Effect of rheology

A comparison of the shapes of three folds with identical starting configuration ($L_o/h_o = 12, A_o = 0.1\,h_o$), the same shortening ($S = 50\%$), and the same viscosity ratio ($m = 100$), but for different values of n_L ($n_L = 1, 3, 10$), is made in Fig. 11. Amplitude (or limb dip) is not the same because the strength of the buckling instability, and thus also growth rate, increases with n_L. It is apparent from this figure that the limbs become relatively longer and straighter as n_L is increased and that the hinges (in both inner and outer arcs) become more localized and sharper. This is borne out by the values of *ki* calculated for the outer arcs of these folds (see caption to Fig. 11). Similar differences in shape are apparent in other models at different values of L_o/h_o (see Lan & Hudleston 1991, fig. 4, for $L_o/h_o = 30$) and for different values of m. (It will be apparent later that n_L is much more important in determining these characteristics of shape than m.)

There are also differences in the pattern of thickness variations around the computer-generated folds that can be associated with differences in n_L. Examples of such differences for linear and non-linear cases are shown in Figs. 12 and 13. For $n_L = 1$ and $m = 10$ hinge thickening (and eventually limb thinning as dips exceed 45°) occurs progressively such that, on a plot of t'_α against α, the fold moves systematically from its initial class 1B (parallel) shape towards a class 2 (similar) shape through the field of class 1C. The data plot very close to the theoretical curves for 'flattened' parallel folds (Ramsay 1967, fig. 7–79) as had been observed earlier in physical experiments in linear viscous materials at low viscosity contrast (Hudleston 1973b). For $L_o/h_o = 6$ the shape after 75% shortening is that of a highly flattened parallel fold. Much less flattening occurs for $L_o/h_o = 20$ (Fig. 13a, the folds shown in Fig. 5). In neither of these cases does the fold actually flatten in the manner proposed by Ramsay (i.e. by homogeneous strain of a parallel fold): for this to happen the viscosities of layer and matrix would need to be the same.

For $n_L = 10$ and $m = 630$ the pattern of thickness

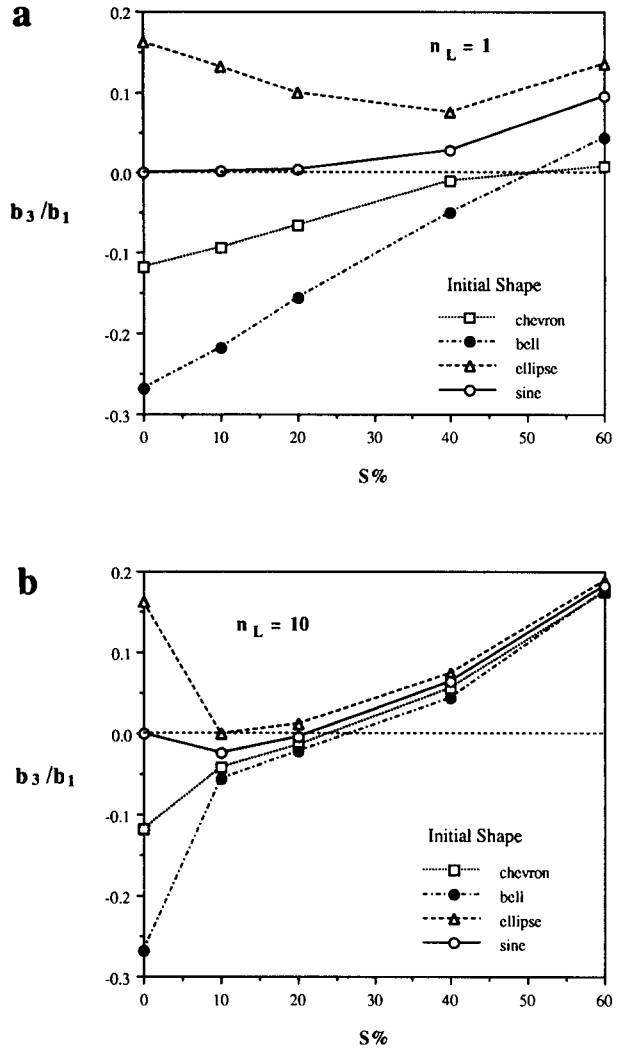

Fig. 8. Harmonic analysis of the outer arc segments (from inflexion point to anticlinal hinge) of the folds developed from the initial perturbations shown in Fig. 6(a), for (a) $n_L = 1$, $m = 10$ and (b) $n_L = 10$, $m = 630$. The dashed line $b_3 = 0$ represents the locus of sine functions.

changes with dip and with shortening is quite different. The most apparent difference is that relative thickening in the hinges is much less for folds at high amplitude for $n_L = 10$ than for folds with $n_L = 1$, largely reflecting the much higher value of m for $n_L = 10$, and thus a much higher buckling instability. The second difference is that the hinge thickening that does occur mostly comes early in the deformation, with only modest further changes at later stages. Thus after 10% shortening the folds are close to being similar (class 2) in shape, and with further shortening limb dips increase with little further change in thickness in either hinge or limb. This has the effect, on the t'_α/α plot, of moving the fold 'horizontally' away from a class 2 shape and into the class 1C field. This is best seen on the plot for $L_o/h_o = 12$ (Fig. 13b). However, it should be noted that after about 30% shortening, the changes in position of the fold on the t'_α/α plot are slight. It should also be pointed out that there is 'noise' in the plots of Figs. 12 and 13, especially for $L_o/h_o = 20$, $n_L = 10$, due to the representation of the fold by straight-line segments joining nodal points in the finite element grid. The fold surfaces were not smoothed before measurements of thickness were made.

For any fold, except a similar fold, the inner and outer arcs have different shapes, although at very low amplitudes, as Fletcher (1979) has shown, similar folds and parallel folds are effectively indistinguishable. Differences in shape of inner and outer arcs of non-similar folds become more pronounced as amplitude increases. Because the outer arc (from hinge point to inflexion point) is longer and better defined in both natural and numerical folds than the inner arc, the focus will be on outer arcs in this study. Harmonic analysis reveals some of the features of the different evolution of shape of folds with different values of n_L. In our models, these differences are most pronounced for $L_o/h_o = 20$ and almost non-existent for $L_o/h_o = 6$. (This is not the most desirable situation, because typical natural fold populations have peak values of L/h of 4–8.) On plots of b_3 against b_1, all folds show the characteristic concave upward form, starting from an initial shape on the line $b_3 = 0$. The slope on these plots increases with b_1 and also generally increases with n_L, but the situation is complicated by the initial behavior when $L_o/h_o = 20$ and n_L is large (Figs. 14b & c). Specifically, when $n_L = 10$, $m = 630$ and $L_o/h_o = 20$, fold shape, which starts out as sinusoidal, develops at first a very slight tendency towards chevron style, that is b_3 is initially negative (this phenomenon was already noted in the section on the effect of initial shape). It is not until the fold attains a limb dip of about 50° that b_3 becomes positive, as the fold shape passes back through sinusoidal to become more rounded in the hinge. For $n_L = 1$ and $m = 10$, b_3 becomes positive at the start of the deformation and the ratio of b_3/b_1 increases monotonically. The folds in this case depart from sinusoidal shapes at about 15° limb dips. Shape evolution for $n_L = 3$ is closer to shape evolution for $n_L = 10$ than for $n_L = 1$.

It can be seen from Fig. 14 that there are two circumstances in which differences in shape are slight. When $L_o/h_o = 6$ there are almost no differences in shape among folds for different n_L, and when folds grow to high amplitudes or limb dips, for any value of L_o/h_o or n_L, there is a convergence of shape (Fig. 14c).

Additional information on shape can be obtained by examining curvature from hinge to hinge in the numerical folds. It is instructive first to compare folds showing extreme variations in shape. This is done in Fig. 15 for $L_o/h_o = 12$, $n_L = 1$, $m = 10$, $S = 60\%$ and $L_o/h_o = 20$, $n_L = 10$, $m = 630$, $S = 50\%$. In the linear case there is a slow change in curvature (dk/dx small) from the anticlinal hinge (outer arc) on the left, an increasing gradient through the inflexion point, and a large gradient to attain the high curvature in the synclinal hinge (inner arc). The pattern for $n_L = 10$ is different in several respects. There is a rapid drop in curvature (dk/dx large) away from the anticlinal hinge and a low gradient at the inflexion point with a section of almost straight limb and zero curvature. The curvature in the outer arc is again less than in the inner arc.

As noted using harmonic analysis (Fig. 14a), there are

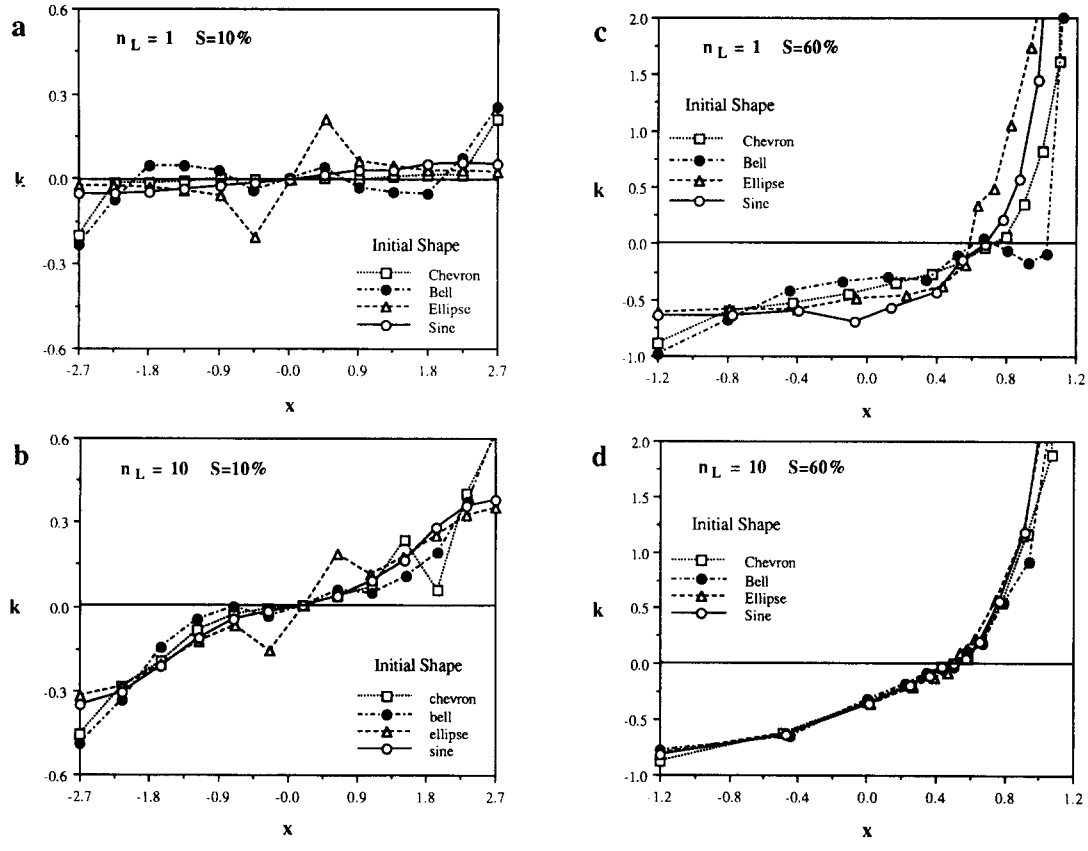

Fig. 9. Curvature as a function of x for the upper surface of folds developed from the initial perturbations shown in Fig. 6(a), after 10% shortening for (a) $n_L = 1$, $m = 10$ and (b) $n_L = 10$, $m = 630$, and after 60% shortening for (c) $n_L = 1$, and for (d) $n_L = 10$.

only slight differences in shape among all the numerical folds produced for $L_o/h_o = 6$ and $n_L = 1$, 3 and 10, and regardless of the value of m. For $L_o/h_o = 20$, however, there are systematic differences in shape of the outer arc, which are reflected in the value of ki, for different values of n_L. ki systematically increases with n_L at all stages of shortening (Fig. 16). Also, ki changes relatively little in value in each case as shortening progresses. Thus, folds are straighter-limbed and sharper-hinged at all stages of folding as n_L is increased, with some convergence of shape at the highest values of S, corresponding to limb dips of 80–90°. The weak dependence of ki on m can be seen in Fig. 16, in which data for several values of m are plotted. Results for $n_L = 3$, $m = 2150$, and for $n_L = 10$, $m = 6300$ are almost indistinguishable from those for $n_L = 3$, $m = 215$ and $n_L = 10$, $m = 630$, respectively, and are not plotted.

Discussion

Experimental models of buckle folds starting with 'flat' layers show a progressive development in shape from low-amplitude sinusoids when first measurable ($b_3 \approx 0$ for outer or inner arc surface shape) to become rounded in the hinges (e.g. Figs. 1 and 2) (see also Hudleston 1973b). Folds in physical and numerical models that take initial perturbations in the layers to be of sinusoidal shape undergo similar shape development (e.g. Fig. 14). Chapple (1969) demonstrated that localized plastic failure in fold hinges would lead to sharper hinges and straighter limbs than the more uniformly distributed strain in folds developed in unconfined Newtonian viscous layers. One might expect that folds in layers with non-linear flow laws might develop mature shapes that tended to become straighter limbed as the exponent in the flow law is increased. This is what we observe in our numerical models.

The early development of a sinusoidal shape reflects the fact that harmonic components of the perturbation to first-order grow independently (Biot 1961, Fletcher 1974) and the fastest growing harmonic dominates the early shape development. Thus for the four different initial perturbations on a primary wavelength displayed in Fig. 6, a comparison of the theoretical and numerical growth rates of the harmonic components (Table 2) shows that for $n_L = 1$ the early growth (A/A_o) of the first and third terms in the cosine series is constant and independent of initial shape, as predicted by theory. The contribution of the term in cos x outpaces that due to the term in cos $3x$, such that the ratio a_3/a_1 (also b_3/b_1) diminishes (except for the sinusoidal function for which a_3 is theoretically initially zero) as the fold grows. This is apparent in Fig. 8. The growth rates are much stronger for $n_L = 10$ than $n_L = 1$, and b_3/b_1 diminishes much more rapidly with shortening in Fig. 8(b) than in Fig. 8(a). Nice experimental verification of the independent low-amplitude growth of the harmonic components of a bell-shaped perturbation has been given by Abbassi & Mancktelow (1992).

Spontaneous modification of a sinusoidal fold shape

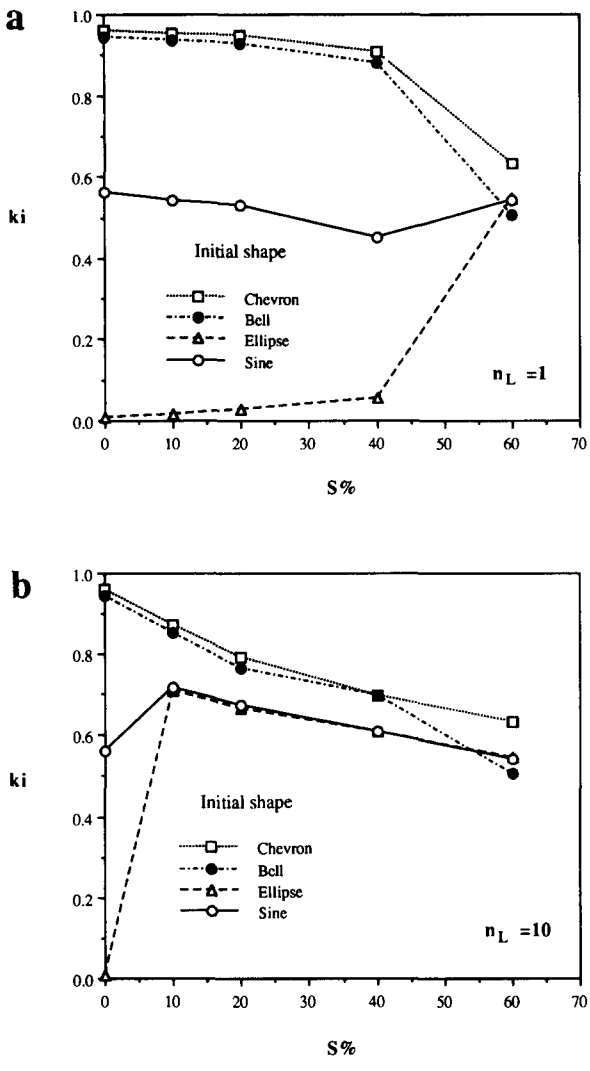

Fig. 10. Change in curvature index, *ki*, with shortening for the outer arc segments (from inflexion point to anticlinal hinge) of the folds developed from the initial perturbations shown in Fig. 6(a), for (a) $n_L = 1$, $m = 10$ and (b) $n_L = 10$, $m = 630$.

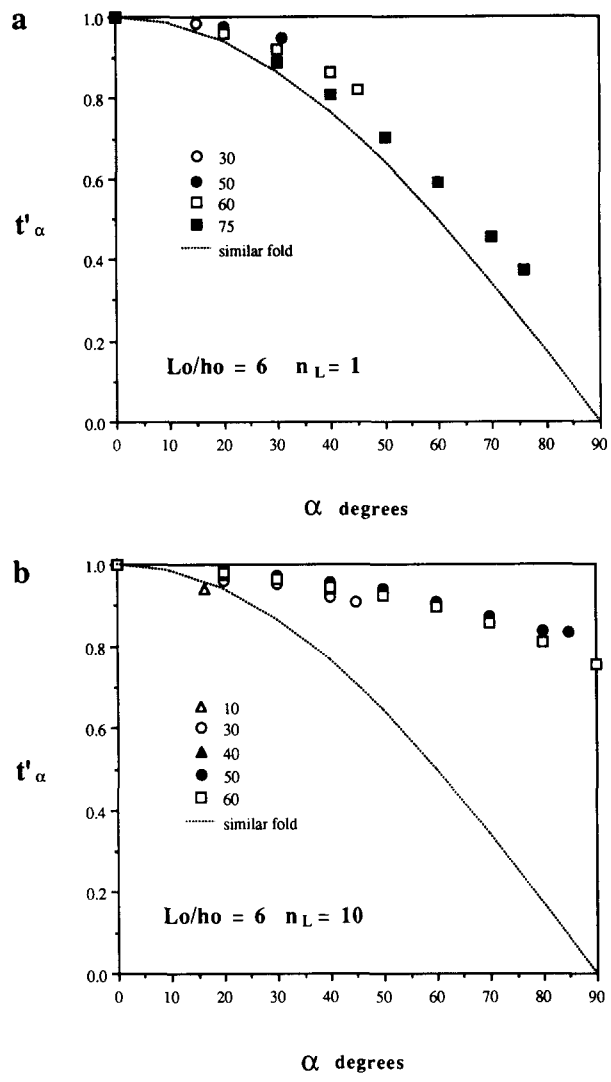

Fig. 12. Folded layer thickness, expressed as $t'_\alpha = t_\alpha/t_o$, as a function of 'dip', α, for numerical model folds with $L_o/h_o = 6$, at various stages of shortening for (a) $n_L = 1$, $m = 10$ and (b) $n_L = 10$, $m = 630$.

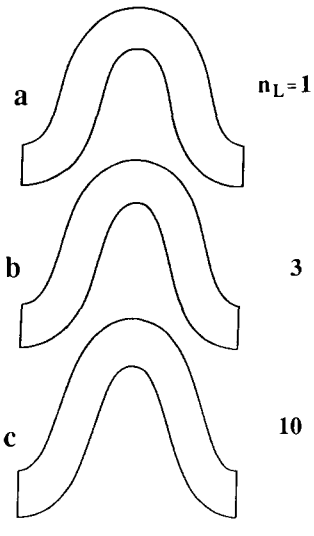

Fig. 11. Comparison of the shapes of mature folds developed from identical initial sinusoidal perturbations ($L_o/h_o = 12$, $A_o = 0.1h_o$) and for the same viscosity ratio ($m = \mu_L/\mu_M = 100$), for three different values of power-law exponent, n_L. All at 50% shortening. (a) $n_L = 1$; $ki = 0.573$; (b) $n_L = 3$, $ki = 0.624$; (c) $n_L = 10$, $ki = 0.691$.

occurs with fold growth and the appearance of higher order harmonics (Fletcher 1979, 1982, Johnson & Pfaff 1989). The first harmonic (term in cos $2x$) provides in all the cases studied here a pinch-and-swell modification (a_2 negative for the upper surface and positive for the lower surface, if a_1 is positive) to the term in cos x, and this has the effect of maintaining an approximate parallel fold shape, up to moderate limb dips (Fletcher 1979). This effect is not examined further here, and is 'hidden' by the use of a sine series to represent fold shapes. The progressive increase in the value of b_3/b_1 with b_1 (or limb dip) shown in Figs. 2 and 14 reflects the modification of the sinusoidal shape given by b_1 by the term in sin $3x$, which gives the folds more rounded hinges. This also occurs in all the cases studied, but to a degree that depends on the value of n_L. The initial decrease in b_3/b_1 in Fig. 8 represents independent growth of the two harmonics, in which the higher order wavelength is amplified less than the 'primary' wavelength; the subsequent increase in b_3/b_1 represents the finite-amplitude effect of shape modification by the term in sin $3x$.

The differences in shape among folds in stiff layers

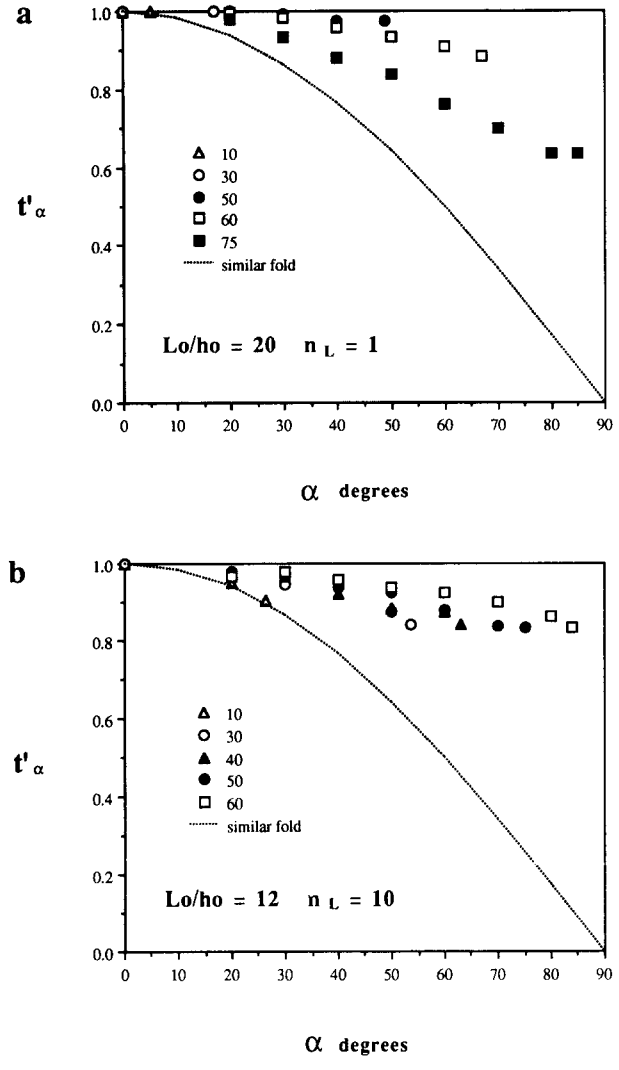

Fig. 13. Thickness for model folds at various stages of shortening and (a) $L_o/h_o = 20$, $n_L = 1$, $m = 10$ and (b) $L_o/h_o = 12$, $n_L = 10$, $m = 630$.

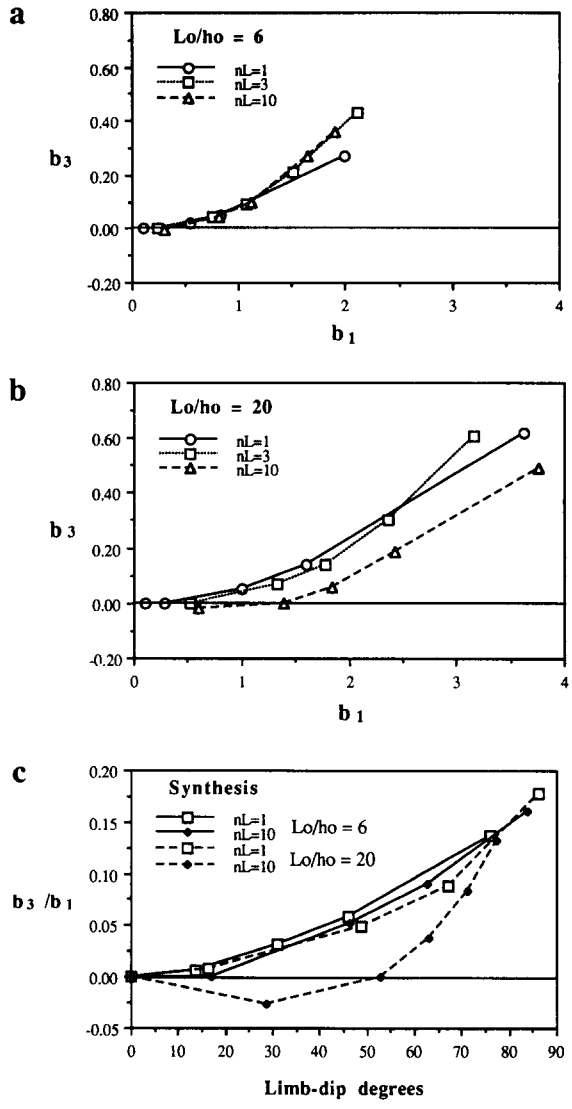

Fig. 14. Harmonic analysis of the outer arc segments (from inflexion point to anticlinal hinge) of computer-generated folds for the conditions shown. In all plots, $n_L = 1, 3, 10$ corresponds to $m = 10, 215, 630$, respectively. Shortening is up to 75% (for $n_L = 1$) or 60% (for other cases). (a) & (b) Plots of b_3 against b_1; (c) plots of b_3/b_1 against limb dip.

with different values of stress exponent, n_L, may be accounted for by variations in effective viscosity around the folded layer due to variations in stresses associated with buckling. The effect of these viscosity variations on the perturbing flow are not accounted for in the analytical expressions of fold growth. Normal stresses in the stiff layer will be highest in the fold hinges, and thus in non-linear stiff layers the hinge zone will be relatively weak in response to layer-parallel buckling stresses. Deformation in the hinges takes the form of shortening in the inner arc and extension in the outer arc with, for non-linear layers, the former exceeding the latter, giving rise to a slight net thickening in the hinges. This preferential 'failure' in the hinges is the cause of the hinge thickening noted in plots of t'_α/α (Fig. 13b) and the reason that the limbs remain relatively straight and tend to rotate bodily, as shown by the curvature distribution (Fig. 15) and the plots of ki vs shortening for different values of n_L (Fig. 16). In the limit when $n_L = \infty$ in an unconfined stiff layer, as Chapple (1969) has shown, there is plastic failure in the hinge and no deformation in the limbs, and a perfect chevron fold develops.

As folds attain high limb dips, much of the work involved in buckling is associated with driving out matrix material from between the fold limbs, and the pattern of deformation does not differ greatly from one of passive folding (i.e. homogeneous flow) (Chapple 1968). At this stage of folding, differences in fold shape for different values of n_L tend to be diminished. Differences in fold shape are also less when L_o/h_o is small. In such cases more of the layer is hinge zone and less limb simply as a result of geometry.

COMPARISON WITH OTHER MODELING STUDIES AND APPLICATION TO NATURAL FOLDS

It is instructive to compare our results with the results of other numerical or experimental studies and with data on natural folds, and it is most appropriate to do this by comparing fold shape characteristics at given values of 'wavelength' and 'amplitude', represented by L/h and

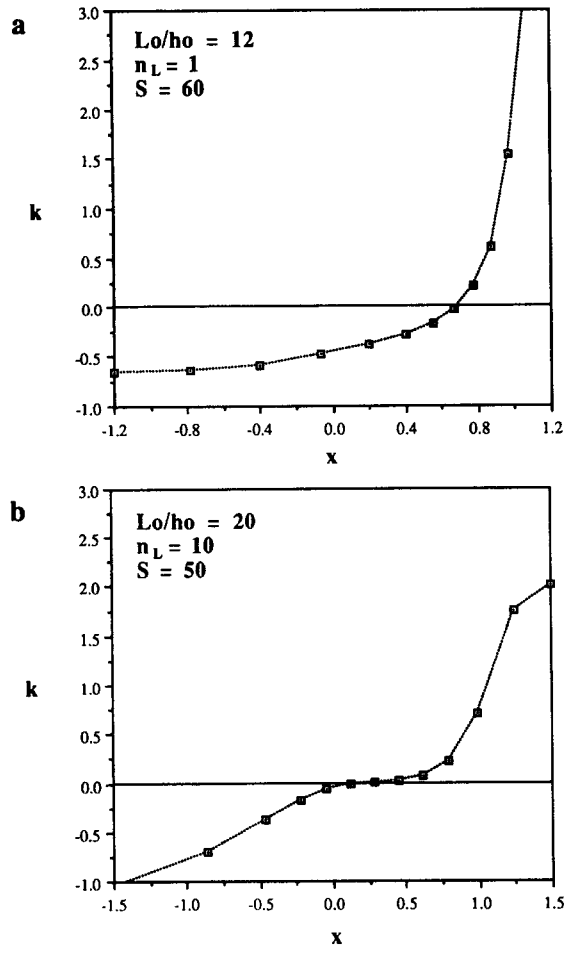

Fig. 15. Curvature, k, in selected computer-generated folds, as a function of (arbitrary) co-ordinate distance, x, from 'anticlinal' hinge or outer arc (left) to 'synclinal' hinge or inner arc (right) for the conditions shown. Note the straight limb segment around the inflection point in (b). The two folds represented in (a) and (b) were selected only to show the strong contrast in pattern of curvature variation.

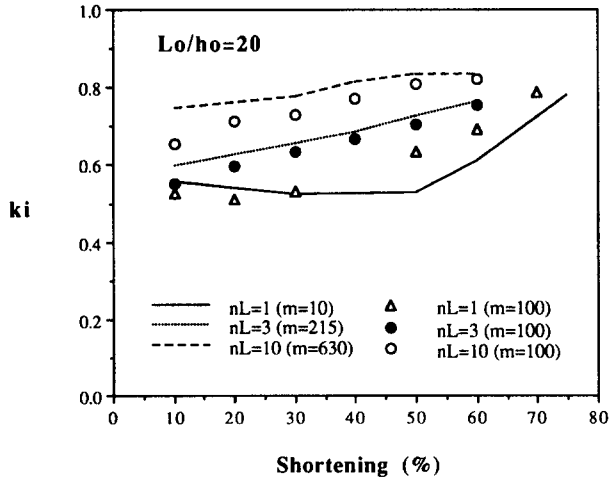

Fig. 16. Variation in curvature index, ki, with shortening, S, for the outer arc segments of computer-generated folds with $L_o/h_o = 20$ and for $n_L = 1, 3, 10$, $m = 100$ and $n_L = 1, 3, 10$, $m = 10, 215, 630$, respectively.

Table 2. Growth of numerical folds represented by the first two terms in a cosine series, for $n_L = 1$, $L_o/h_o = 12$, $m = 10$, and for four initial shapes (see Figs. 6 and 7), after 5% shortening. The theoretical values of fold growth from Fletcher's (1974) first-order theory are $a_{1_{S=5}}/a_{1_{S=0}} = 1.27$ and $a_{3_{S=5}}/a_{3_{S=0}} = 1.17$

Initial shape	$a_{1_{S=0}}$	$a_{3_{S=0}}$	$\frac{a_{1_{S=5}}}{a_{1_{S=0}}}$	$\frac{a_{3_{S=5}}}{a_{3_{S=0}}}$
Sine	0.0524	0.00002	1.33	2.39
Chevron	0.0424	0.0048	1.32	1.21
Bell	0.0358	0.0094	1.32	1.21
Ellipse	0.0593	−0.0097	1.32	1.21

limb dip, respectively. Thus, we have interpolated the results of our numerical models to construct diagrams to show how curvature index, ki, varies as a function of L/h for constant limb dip and how ki varies as a function of limb dip for fixed L/h, for various values of n_L.

It was noted earlier in the paper that the largest differences in shape among folds for different values of n_L are for intermediate stages of fold development and for large values of L_o/h_o. Therefore we plot ki as a function of L/h for maximum limb dips of 40° (Fig. 17a) and 70° (Fig. 17b), and ki as a function of limb dip for $L/h = 12$ (Fig. 18). The interpolated data points are joined by solid lines on these figures. For our numerical data, there is a strong increase in ki with L/h up to about $L/h = 10$, and a modest increase thereafter. For $L/h > 10$, ki is systematically larger for increasing values of n_L, but for $L/h \leq 10$ there is no clear pattern of dependence of ki on n_L. In Fig. 18 note that ki changes very little with limb dip for constant L/h and again that higher values of ki are associated with larger values of n_L. Within the range of viscosity ratios studied and for $L/h \geq 10$ there is only a weak dependence of ki on m, with ki increasing as m is increased (see Fig. 16). Thus, only the results for $m = 100$ are plotted in Figs. 17 and 18.

Other modeling results

Data for selected numerically- and experimentally-produced folds from other studies are plotted as individual points on Figs. 17(a) and 18. Because there is such a weak dependence of ki on L/h and limb dip (for $L/h > 10$) data are plotted on these figures if limb dip is 40° ± 5° (Fig. 17a) and $L/h = 12 \pm 2$ (Fig. 18). The experiments carried out by Hudleston (1973b) and the numerical models of Cruikshank & Johnson (1993) utilized Newtonian materials, and the data for these plot close to the line for $n_L = 1$. For all the experiments using non-linear materials, the data are consistent with highly non-linear behavior. The power-law exponents for the limestone and marble used in the experiments of Gairola & Kern (1984) are not known, but are likely to be high ($n_L > 3$). In Cobbold's (1975) and Neurath & Smith's (1982) experiments, n_L for the stiff layer was measured as 2.6 and 5, respectively. Growth rates in Neurath & Smith's experiments were unexpectedly high, perhaps, as the authors suggest, due to strain softening. This would result in an 'effective' power-law exponent higher than the measured value (Neurath & Smith 1982).

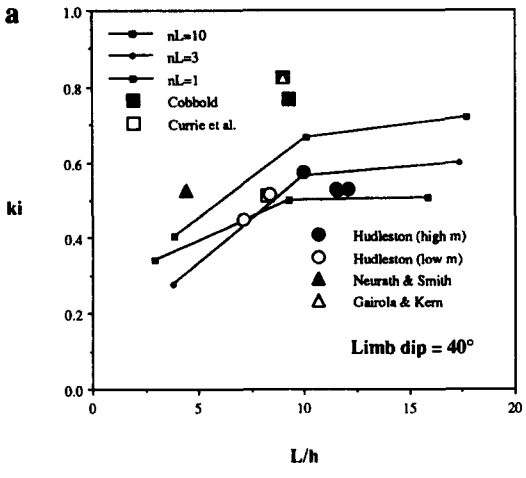

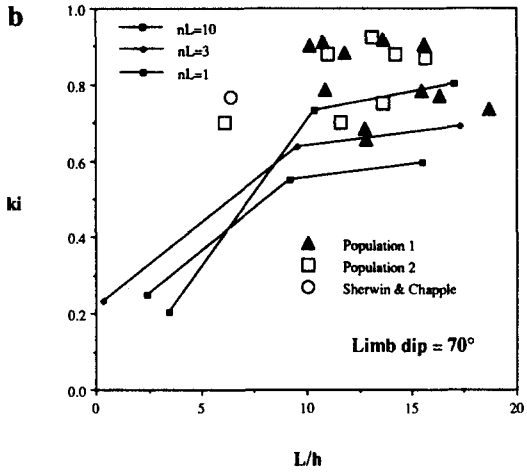

Fig. 17. Curvature index, *ki*, as a function of *L/h* at fixed limb dip interpolated from results of numerical fold models with *L/h* = 6, 12, 20, n_L = 1, 3, 10 and *m* = 100. (a) Limb dip = 40° and (b) limb dip = 70° (cf. Hudleston & Lan 1993, fig. 13a). Selected data for experimentally-produced folds (Currie *et al.* 1962, Hudleston 1973b, Cobbold 1975, Neurath & Smith 1982, Gairola & Kern 1984) and natural folds (Sherwin & Chapple 1968, and two sets of data from folds in siltstones in shales in the central Appalachians—populations 1 and 2) are plotted for comparison. See text for discussion.

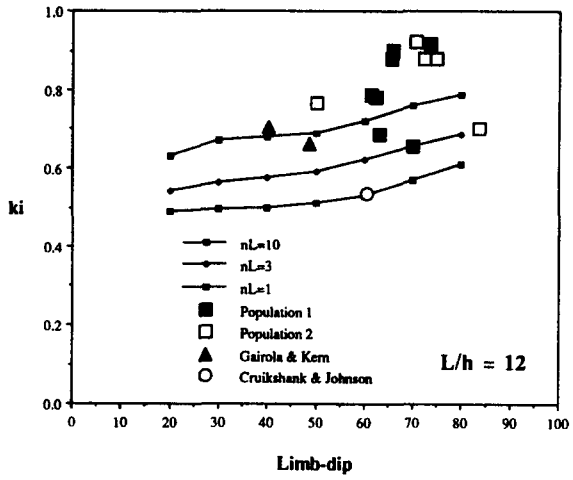

Fig. 18. Curvature index, *ki*, as a function of limb dip interpolated from results of numerical fold models with *L/h* = 6, 12, 20, n_L = 1, 3, 10 and *m* = 100 (cf. Hudleston & Lan 1993, fig. 13b). Two sets of data from folds in siltstones in shales in the central Appalachians (populations 1 and 2), one set of data from experimentally-produced folds in limestone (Gairola & Kern 1984) and data for other numerically-produced folds (for *m* = 100, n_L = 1) (Cruikshank & Johnson 1993) are plotted for comparison. See text for discussion.

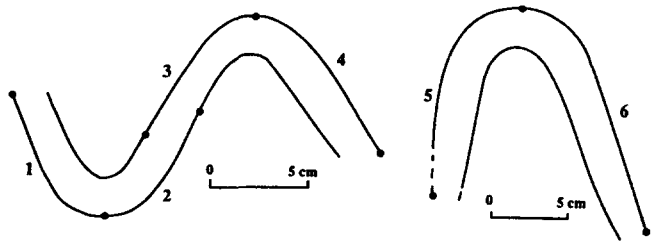

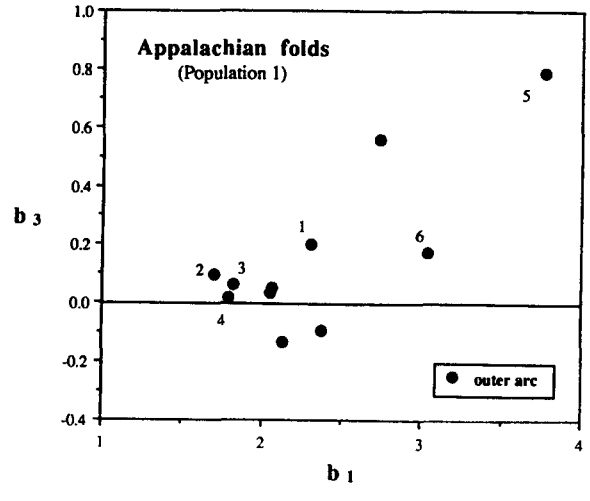

Fig. 19. Representative folds in fine sandstone–siltstone layers in shales of the Trimmer's Rock Formation, Pennsylvania, and their representation (with other folds from the same outcrop) on a plot of harmonic components. Only outer arcs are plotted. Hinges and inflection points are indicated for the numbered folds. Curvature indices for some of these folds are plotted on Figs. 17 and 18. The folds occur in a roadcut about 1 km north of the Watts exit on U.S. Highway 22.

Natural folds

Data for natural folds are plotted in Figs. 17(b) and 18. Again, because there is such a weak dependence of *ki* on *L/h* and limb dip, data are plotted on these figures if limb dip is 70° ± 5° (Fig. 17b) and *L/h* = 12 ± 2 (Fig. 18). The natural data come from the study of Sherwin & Chapple (1968) and from our own work on small folds from the Valley and Ridge province of the central Appalachians. The latter folds are developed in thin layers of fine-grained sandstone–siltstone in shale of the Trimmer's Rock Formation, southeast Pennsylvania. They can be characterized as occurring in layers isolated from their neighbors: representative examples are shown in Fig. 19. The data for these folds cluster in a field in Fig. 17(b) or Fig. 18 that ranges from about n_L = 3 to well above the line for n_L = 10.

Experimental work suggests that the exponent in the flow law for most rocks undergoing deformation controlled by crystal-plastic deformation mechanisms is in the range $2 \leq n_L \leq 7$ (e.g. Kirby & Kronenberg 1987).

Most of the data for the natural folds in Figs. 17(b) and 18 imply $n_L > 10$. The unexpectedly high values of n_L inferred for the natural folds suggest that other factors, such as strain softening or anisotropy, may be influencing fold shape. Neurath & Smith (1982) showed that strain softening may be considered, to a first approximation, equivalent to increasing the effective power-law exponent in the flow law, and Cobbold (1976) and Ridley & Casey (1989) have shown that anisotropy can lead to instabilities and growth of sharp-hinged folds (thus having high values of *ki*). Further consideration of these possibilities is beyond the scope of this paper. It should also be stated here that there is considerable uncertainty about the flow laws appropriate to natural conditions, for a number of reasons. These include the wide range of values of flow law constants reported in experiments (Kirby & Kronenberg 1987) and the fact that most rocks are polymineralic and more complex rheologically than the monomineralic rocks typically tested (Handy 1990).

Variability of fold shape

It is clear from the data plotted in Figs. 17 and 18 and for other types of data representing shapes of natural folds (e.g. Hudleston 1973c, Ramsay & Huber 1987, figs. 15.31 and 19.8) that there is a lot of 'noise' in natural fold systems. This is not surprising considering that the surfaces of layers that develop natural folds often have irregularities that are up to 0.1 of layer thickness. Although our numerical simulations show a weak dependence of final shape on initial shape, in each case there is a 'primary' harmonic that controls shape development. This will not always be the case for natural perturbations, and it is common in nature to see the effects of superimposed wavelengths in a mature fold train. The most obvious examples of this can be avoided in analysis, but the final fold train is inherently noisy, being the result of the operation of the amplification spectra on the initial amplitude spectra (Fletcher & Sherwin 1978).

Abbassi & Mancktelow (1990) examined the case of an initial asymmetric perturbation and showed that the asymmetry was preserved and even amplified in the final fold shape. Local asymmetry of the kind produced in their experiments is fairly common in otherwise symmetric fold trains in nature. It is interesting to note that despite the asymmetry of the folds in Abbassi & Mancktelow's experiments, the two 'halves' of the fold (that is segments from hinge to inflexion points) have similar shapes as represented on harmonic analysis or *ki* plots. Either half represented on a plot of the type shown in Figs. 17 and 18 could thus reflect the rheology quite well. We find values of curvature index of between 0.6 and 0.7 for both symmetric and asymmetric folds (with limb dips of 75–80° and $L/h \cong 7$–10) of Abbassi & Mancktelow (1990, fig. 2). In our numerical models these correspond to values of n_L of $\approx$ 5–7, roughly equivalent to what Abbassi & Mancktelow inferred the effective stress exponent to be in their experiments.

Conclusion

The results of the numerical experiments presented in this paper and a comparison of their shape characteristics with those of experimentally-produced folds give support to the notion that it may be possible to use shape to make inferences about the rheological properties of rocks during folding in nature. Information on rheology obtained from a study of fold geometry, although incomplete and with significant uncertainty attached, complements information obtained from experimental rock deformation and analysis of microfabric. From the limited data now available, there seems to be mutual consistency among these different approaches, in indicating non-linear material behavior, but inconsistency in the degree of non-linearity indicated.

Acknowledgements—This work was supported by grants from the National Science Foundation (EAR 8804670 and 9017922) and the University of Minnesota Supercomputer Institute. The manuscript has been greatly improved as a result of reviews by Arvid Johnson, Neil Mancktelow and Sue Treagus. Correspondence with Ray Fletcher has also been most useful to us in revising the paper.

REFERENCES

Abbassi, M. R. & Mancktelow, N. S. 1990. The effect of initial perturbation shape and symmetry on fold development. *J. Struct. Geol.* **12**, 273–282.

Abbassi, M. R. & Mancktelow, N. S. 1992. Single-layer buckling in non-linear materials—I. Experimental study of fold development from an isolated initial perturbation. *J. Struct. Geol.* **14**, 85–104.

Bastida, F. 1993. A new method for the geometrical classification of large data sets of folds. *J. Struct. Geol.* **15**, 69–78.

Biot, M. A. 1957. Folding instability of a layered viscoelastic medium under compression. *Proc. R. Soc. Lond.* **A242**, 444–454.

Biot, M. A. 1961. Theory of folding of stratified viscoelastic media and its implications in tectonics and orogenesis. *Bull. geol. Soc. Am.* **72**, 1595–1620.

Biot, M. A., Odé, H. & Roever, W. L. 1961. Experimental verification of the folding of stratified viscoelastic layers. *Bull. geol. Soc. Am.* **72**, 1621–1630.

Chapple, W. M. 1968. A mathematical theory of finite-amplitude rock-folding. *Bull. geol. Soc. Am.* **79**, 47–68.

Chapple, W. M. 1969. Fold shape and rheology: the folding of an isolated viscous-plastic layer. *Tectonophysics* **7**, 97–116.

Cobbold, P. R. 1975. Fold propagation in single embedded layers. *Tectonophysics* **27**, 333–351.

Cobbold, P. R. 1976. Mechanical effect of anisotropy during large finite deformation. *Bull. Soc. Géol. Fr.*, 7 *Ser.* **18**, 1497–1510.

Cobbold, P. R., Cosgrove, J. W. & Summers, J. M. 1971. Development of internal structures in deformed anisotropic rocks. *Tectonophysics* **12**, 23–53.

Cruikshank, K. M. & Johnson, A. M. 1993. Simulation of high-amplitude folding in viscous multilayers. *J. Struct. Geol.* **15**, 79–94.

Currie, J. B., Patnode, H. W. & Trump, R. P. 1962. Development of folds in sedimentary strata. *Bull. geol. Soc. Am.* **73**, 655–674.

Fletcher, R. C. 1974. Wavelength selection in the folding of a single layer with power-law rheology. *Am. J. Sci.* **274**, 1029–1043.

Fletcher, R. C. 1979. The shape of single-layer folds at small but finite amplitude. *Tectonophysics* **60**, 77–87.

Fletcher, R. C. 1982. Analysis of the flow in layered fluids at small, but finite, amplitude with application to mullion structures. *Tectonophysics* **81**, 51–66.

Fletcher, R. C. & Sherwin, J. 1978. Arc length of single layer folds: a

discussion of the comparison between theory and observation. *Am. J. Sci.* **278**, 1085–1098.
Fleuty, M. J. 1964. The description of folds. *Proc. Geol. Ass.* **75**, 461–492.
Gairola, V. K. & Kern, H. 1984. Single-layer folding in marble and limestone: an experimental study. *Tectonophysics* **108**, 155–172.
Handy, M. R. 1990. The solid-state flow of polymineralic rocks. *J. geophys. Res.* **95**, 8647–8661.
Hanson, B. H. 1985. Climatic sensitivity of a numerical model of ice-sheet dynamics. Unpublished Ph.D. thesis, University of Minnesota.
Hanson, B. H. 1990. Thermal response of a small ice cap to climatic forcing. *J. Glaciol.* **36**, 48–56.
Holst, T. B. 1987. Analysis of buckle folds from the early Proterozoic of Minnesota. *Am. J. Sci.* **287**, 612–634.
Hudleston, P. J. 1973a. Fold morphology and some geometrical implications of theories of fold development. *Tectonophysics* **16**, 1–46.
Hudleston, P. J. 1973b. An analysis of single layer folds developed experimentally in viscous media. *Tectonophysics* **16**, 189–214.
Hudleston, P. J. 1973c. The analysis and interpretation of minor folds developed in the Moine rocks of Monar, Scotland. *Tectonophysics* **17**, 89–132.
Hudleston, P. J. & Holst, T. B. 1984. Strain analysis and fold shape in a limestone layer and implications for layer rheology. *Tectonophysics* **106**, 321–347.
Hudleston, P. J. & Lan, L. 1993. Information from fold shapes. *J. Struct. Geol.* **15**, 253–264.
Hudleston, P. J. & Tabor, J. R. 1988. Strain and fabric development in a buckled calcite vein. *Bull. Geol. Inst., Univ. Uppsala, N.S.* **14**, 79–94.
Johnson, A. M. & Pfaff, V. J. 1989. Parallel, similar and constrained folds. *Engng Geol.* **27**, 115–180.
Kincaid, D. & Cheney, W. 1991. *Numerical Analysis*. Brooks/Cole Publishing, Pacific Grove, California.
Kirby, S. H. & Kronenberg, A. K. 1987. Rheology of the lithosphere: selected topics. *Rev. Geophys.* **23**, 1219–1244.
Lan, L. & Hudleston, P. J. 1991. Finite element models of buckle folds in non-linear materials. *Tectonophysics* **199**, 1–12.
Leithold, L. 1981. *The Calculus With Analytic Geometry*. Harper & Row, New York.
Lisle, R. J. 1992. Constant bed-length folding: three-dimensional geometrical implications. *J. Struct. Geol.* **14**, 245–252.
Mancktelow, N. S. & Abbassi, M. R. 1992. Single-layer buckling in non-linear materials—II. Comparison between theory and experiment. *J. Struct. Geol.* **14**, 105–120.
Mertie, J. B. 1959. Classification, delineation and measurement of non-parallel folds. *Prof. Pap. U.S. geol. Surv.* **314E**, 91–124.
Neurath, C. & Smith, R. B. 1982. The effect of material properties on growth rates of folding and boudinage: experiments with wax models. *J. Struct. Geol.* **4**, 215–229.
Ramberg, H. 1961. Relationship between concentric longitudinal strain and concentric shearing strain during folding of homogeneous sheets of rock. *Am. J. Sci.* **259**, 382–390.
Ramberg, H. 1963a. Strain distribution and geometry of folds. *Bull. Geol. Inst. Univ. Uppsala* **42**, 1–20.
Ramberg, H. 1963b. Fluid dynamics of viscous buckling applicable to folding of layered rocks. *Bull. Am. Ass. Petrol. Geol.* **47**, 484–505.
Ramberg, H. 1970. Folding of compressed multilayers in the field of gravity I, II. *Phys. Earth & Planet. Interiors* **2**, 203–232; **4**, 83–120.
Ramsay, J. G. 1967. *Folding and Fracturing of Rocks*. McGraw Hill, New York.
Ramsay, J. G. & Huber, M. I. 1987. *The Techniques of Modern Structural Geology, Volume 2: Folds and Fractures*. Academic Press, London.
Ridley, J. & Casey, M. 1989. Numerical modeling of folding in rotational strain histories: strain regimes expected in thrust belts and shear zones. *Geology* **17**, 875–878.
Sherwin, J. & Chapple, W. M. 1968. Wavelengths of single-layer folds: a comparison between theory and observation. *Am. J. Sci.* **266**, 167–179.
Smith, R. B. 1975. Unified theory of the onset of folding, boudinage, and mullion structure. *Bull. geol. Soc. Am.* **86**, 1601–1609.
Smith, R. B. 1977. Formation of folds, boudinage, and mullions in non-Newtonian materials. *Bull. geol. Soc. Am.* **88**, 312–320.
Stabler, C. L. 1968. Simplified Fourier analysis of fold shapes. *Tectonophysics* **6**, 343–350.
Twiss, R. J. 1988. Description and classification of folds in single surfaces. *J. Struct. Geol.* **10**, 607–623.
Van Hise, C. R. 1896a. Studies for students. Deformation of rocks. *J. Geol.* **4**, 195–213.
Van Hise, C. R. 1896b. Studies for students. Deformation of rocks, Part II. *J. Geol.* **4**, 312–353.
Wilson, G. 1967. The geometry of cylindrical and conical folds. *Proc. Geol. Ass.* **78**, 179–200.
Wollkind, D. J. & Alexander, J. I. D. 1982. Kelvin–Helmholtz instability in a layered Newtonian fluid model of the geological phenomenon of rock folding. *J. Appl. Math.* **42**, 1276–1295.